

Allosteric Signal within the Receptor-Binding Domain of the SARS-CoV-2 Spike Protein Mediated by a Class 3 Monoclonal Antibody Revealed through Molecular Dynamics Simulations and Protein Residue Networks

Patamalai Boonserm, Wasusit Somsoros, Pongsak Khunrae, Krit Charupanit, Praopim Limsakul, and Thana Sutthibutpong*



Cite This: *ACS Omega* 2024, 9, 4684–4694



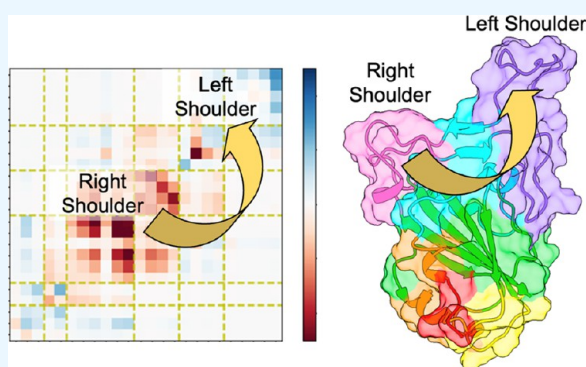
Read Online

ACCESS |

Metrics & More

Article Recommendations

ABSTRACT: This study investigated the allosteric action within the receptor-binding domain (RBD) of the SARS-CoV-2 spike protein caused by class 3 monoclonal antibody (mAb) binding. As the emergence of SARS-CoV-2 variants has raised concerns about the effectiveness of treatments by antibodies, targeting the highly conserved class 3 epitopes has become an alternative strategy of antibody design. Simulations of explicitly solvated RBD of the BA.2.75 omicron subvariants were carried out both in the presence and in the absence of bebtelovimab, as a model example of class 3 monoclonal antibodies against the RBD of the SARS-CoV-2 spike protein. The comparative analysis showed that bebtelovimab's binding on two α helices at the epitope region disrupted the nearby interaction network, which triggered a denser interaction network formation on the opposite side of the receptor-binding motif (RBM) region and resulted in a “close” conformation that could prevent the ACE2 binding. A better understanding of this allosteric action could lead to the development of alternative mAbs for further variants of concern. In terms of computational techniques, the communicability matrix could serve as a tool to visualize the effects of allostery, as the pairs of amino acids or secondary structures with high communicability could pinpoint the possible sites to transfer the allosteric signal. Additionally, the communicability gain/loss matrix could help elucidate the consequences of allosteric actions, which could be employed along with other allostery quantification techniques in some previous studies.



1. INTRODUCTION

Over 3 years of the COVID-19 pandemic, the World Health Organization (WHO) recently announced that it is no longer an international public health emergency on May 2023, which could turn COVID-19 into the endemic phase because its presence becomes steadier and more predictable in a particular region. However, the SARS-CoV-2 coronavirus has still evolved, leading to a significant number of mutated variants of concern (VOCs) that continue to affect the global population.¹ Therefore, antiviral agents, such as small inhibitors, antibodies, and vaccines, are still being continuously developed against new VOCs.² The spike (S) glycoprotein of SARS-CoV-2 has been one of the main targets for drug development, as its interaction with the human angiotensin-converting enzyme 2 (ACE2) initiates viral infection. Each S protein protomer is composed of two functional subunits; the S1 subunit is responsible for binding to the host receptor and contains an N-terminal domain (NTD) and a receptor-binding domain (RBD);³ the S2 subunit is responsible for facilitating

viral cell membrane fusion through the membrane fusion machinery.⁴ Binding of the trimeric S protein onto ACE2 only occurs when at least one RBD of the S1 subunit from the trimer is elevated and rotated away from the S2 subunit to expose its receptor-binding surface.^{5,6} Figure 1a displays a 3D structure of an RBD protein that resembles an outward-facing human body, along with nomenclatures of the protein regions for parts of the body. Inhibitors that target S glycoproteins typically prevent virus–membrane fusion by interfering with the interaction between RBD and ACE2 (see Figure 1b) as analogous to the body carrying an object on the shoulder.⁷

Received: October 11, 2023

Revised: December 26, 2023

Accepted: January 3, 2024

Published: January 18, 2024



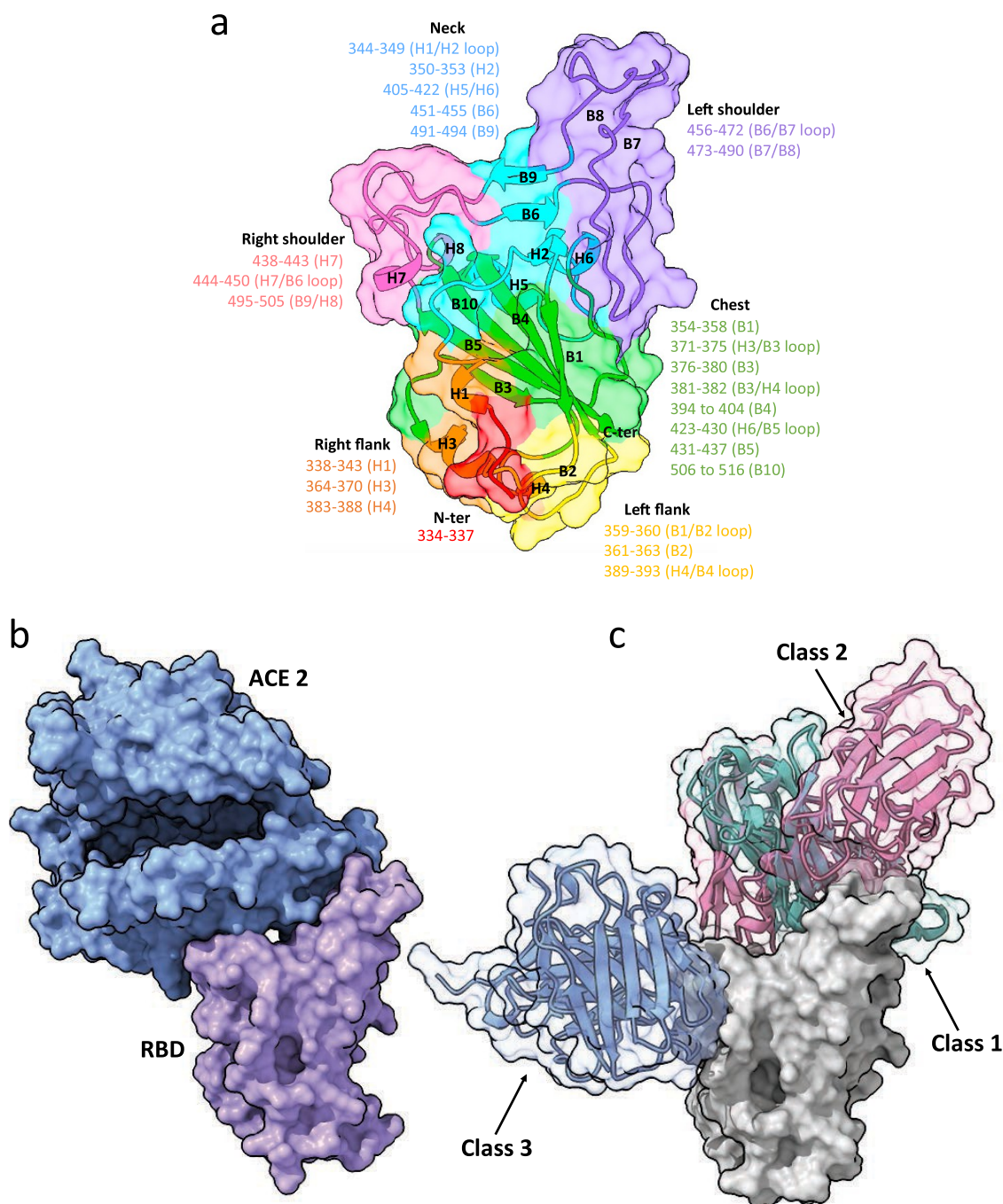


Figure 1. (a) Nomenclatures for different regions and secondary structures of a receptor-binding domain (RBD) of SARS-CoV-2 spike proteins, (b) conformation of an RBD/ACE2 complex obtained from the protein databank (PDB ID: 6M0J), and (c) an RBD domain with superimposed binding configurations of class 1–3 antibodies at different epitopes.

Monoclonal antibodies (mAbs) that specifically target the RBD have become the potential alternative treatments due to their overall effectiveness and safety.^{8,9} These antibodies function by blocking virus's entry into host cells, thereby preventing infection and limiting viral burden.¹⁰ From the structural insight on the RBD/ACE2 binding, the receptor-binding motif (RBM) within the RBD of the SARS-CoV-2 spike protein exhibits sequence variability among sarbecoviruses¹¹ and is where substitutions associated with VOCs and variants of interest (VOIs) tend to accumulate.¹² These substitutions and detectable cross-variant neutralization reduce the efficacy of vaccines and therapeutic mAbs, especially the

omicron VOCs.¹³ Figure 1c shows that class 1 and class 2 antibodies target the less conserved RBM spanning over the “neck” and the “left shoulder” regions, which directly overlap with the binding surface for the ACE2 receptor.¹⁴ Epitopes targeted by the class 3 antibodies, on the other hand, are more conserved than those targeted by class 1 and class 2 antibodies.¹⁵ Thus, the use of class 3 antibodies, e.g., bebtelovimab, is with some advantages over the class 1 and class 2 antibodies because (i) the epitope on the RBD surface for class 3 antibodies contains relatively conserved amino acids compared with other regions in the RBM¹⁶ and (ii) the epitope is exposed for mAbs's binding either at the “closed” or

“opened” RBD states.¹⁷ A deep mutational scanning study suggested that mutations at the bebtelovimab binding residues 444–446 and 499–500 resulted in the complete antibody escape found in XBB and BQ.1 variants,¹⁸ which led to the revocation of emergency use authorization for bebtelovimab in the United States¹⁹ and posed further challenges on the development of new vaccines and neutralizing antibodies due to multiple spike protein mutations.^{20–22} However, as the BA.2, BA.4, and BA.5 omicron subvariants still contained the conserved residues 444–446 and 499–500 outside the heavily mutated regions of RBD,²³ bebtelovimab still displayed its neutralizing efficacy against those subvariants, including the recently emerged BA.2.75.2.^{18,20,24}

As the interactions between bebtelovimab and RBD occurred outside of the RBM region for ACE2, the indirect inhibition mechanism should involve protein dynamics and allosteric signals inside the RBD. The concept of allostery for the communication of mechanical signals between different domains within the SARS-CoV-2 spike protein was previously proposed for the development of allosteric drugs that avoid escape mutations through noncompetitive inhibitions.²⁵ In this study, conformational and network topology analyses were performed using atomistic molecular dynamics (MD) simulations to visualize the short-range allosteric signal within the RBD domain that occurred through the binding of RBD with bebtelovimab. Communicability between secondary structures was defined and compared to the dynamic structural data generated through atomistic MD simulations to provide further interpretation of the mechanical signal transfer that could affect the RBD binding with the ACE2 receptor. Understanding this allosteric action inside the RBD upon antibody binding provided guidance for the choices of class 3 mAbs and for the development of alternative mAbs against some specific variants.

2. METHODOLOGY

2.1. Atomistic Molecular Dynamics (MD) Simulations and Analysis. Three-dimensional coordinates of the SARS-CoV-2 spike receptor-binding domain (RBD; PDB ID 6M0J²⁶) and the RBD/bebtelovimab complex (PDB-ID 7MMO²⁷) were obtained from the crystallographic data provided by the RCSB Protein Data Bank.²⁸ A homology model of RBD and the RBD/bebtelovimab complex with all mutations from BA.2.75.2 was then created and used as starting structures for MD simulations. For each MD simulation performed by the GROMACS2020.3 package,²⁹ proteins and water molecules were parametrized through the GROMOS54A7 force field.³⁰ Then, a dodecahedral simulation box was constructed to cover the whole protein or complex with a 1.0 nm buffer distance to avoid self-contact across the periodic boundaries. After that, an amount of Na⁺ or Cl⁻ ions was added to neutralize the total charge of the simulation box at pH 7 before the whole system underwent energy minimization by the steepest descent algorithm. Simulated annealing was then performed on the energy-minimized system to linearly increase the temperature from 100 to 300 K within 1 ns. Finally, three replicas of 100 ns production MD runs were performed within an NPT ensemble at a constant temperature of 300 K and a constant pressure of 1 atm for both RBD with and without bebtelovimab. Nomenclatures of the MD replicas were given as RBD-r0, RBD-r1, and RBD-r2 for RBD simulations without bebtelovimab binding and as RBD + beb-r0, RBD + beb-r1, and RBD + beb-r2 for RBD simulations

with bebtelovimab binding. The velocity-rescale³¹ and the Berendsen barostat³² algorithms were used to regulate the temperature and pressure, respectively.

When the simulation was finished, all water molecules and ions were removed. Translational and rotational motions were then removed so that only internal motions of proteins were considered. After that, a root-mean-square deviation (RMSD) calculation on the C- α atoms of the RBD part relative to the starting structure was performed to monitor overall conformational dynamics and equilibration, and the per-residue root-mean-square fluctuation (RMSF) was performed over the equilibrated period to assess the flexibility of different RBD regions before and after binding with bebtelovimab. Finally, the middle snapshot of the cluster of equilibrated RBD/bebtelovimab conformations from all three replicas was taken for an interaction analysis by Ligplot 2.2 software,³³ which displayed pairs of amino acids from RBD and bebtelovimab that formed either hydrogen bonds or hydrophobic contacts. Principal component analysis (PCA) was then performed on an ensemble of equilibrated RBD structures from all simulation replicas with and without bebtelovimab binding before each of the RBD trajectories was projected onto the first four eigenvectors.

2.2. Network Topology Analysis. A Python script with commands from the “MDAnalysis” library³⁴ was created to obtain the atomic coordinates of all C- α atoms of both RBD and proteins. The extracted coordinates were defined as “nodes” for the protein residue network (PRN). Then, the “Edges” of the network were defined through any node pairs separated by the distance shorter than the $r_0 = 7.4$ Å cutoff, which represented the effective distance of pairwise interactions between amino acids. The choice of a 7.4 Å cutoff distance was from the distance of the first of the radial distribution function (RDF) shell measured between all C- α pairs, excluding the neighboring pairs connected by peptide bonds. Considering all pairs of amino acids i and j , an element $A_{ij}(t)$ of the adjacency matrix $A(t)$ for PRN at a time step t was defined by

$$A_{ij}(t) = H(r_0 - r_{ij}) = \begin{cases} 1, & r_{ij} < r_0 \\ 0, & r_{ij} \geq r_0 \end{cases} \quad (1)$$

where r_{ij} is the distance between pairs of amino acids i and j . The adjacency matrix $A(t)$ also represented a hopping of any signal between each “adjacent” residue pair when considered as a matrix operation. Therefore, $A^n(t)$ should also represent n hopping steps, and each element of $A^n(t)$ was the number of ways that the signal could transmit between pairs of amino acids i and j , given n hopping steps. Then, a communicability matrix $G(t)$ was defined by the exponential of an adjacency matrix and rewritten as a power series by³⁵

$$G(t) = \exp(A(t)) = \sum_{n=0}^{\infty} \frac{A^n(t)}{n!} = \hat{I} + A(t) + \frac{A^2(t)}{2!} + \frac{A^3(t)}{3!} + \dots \quad (2)$$

According to eq 2, $G(t)$ could be roughly interpreted as the weighted sum of the number of possible paths requiring n hopping steps weighted out by $n!$, which could be roughly interpreted as the loss of mechanical signal for long-distance communication.

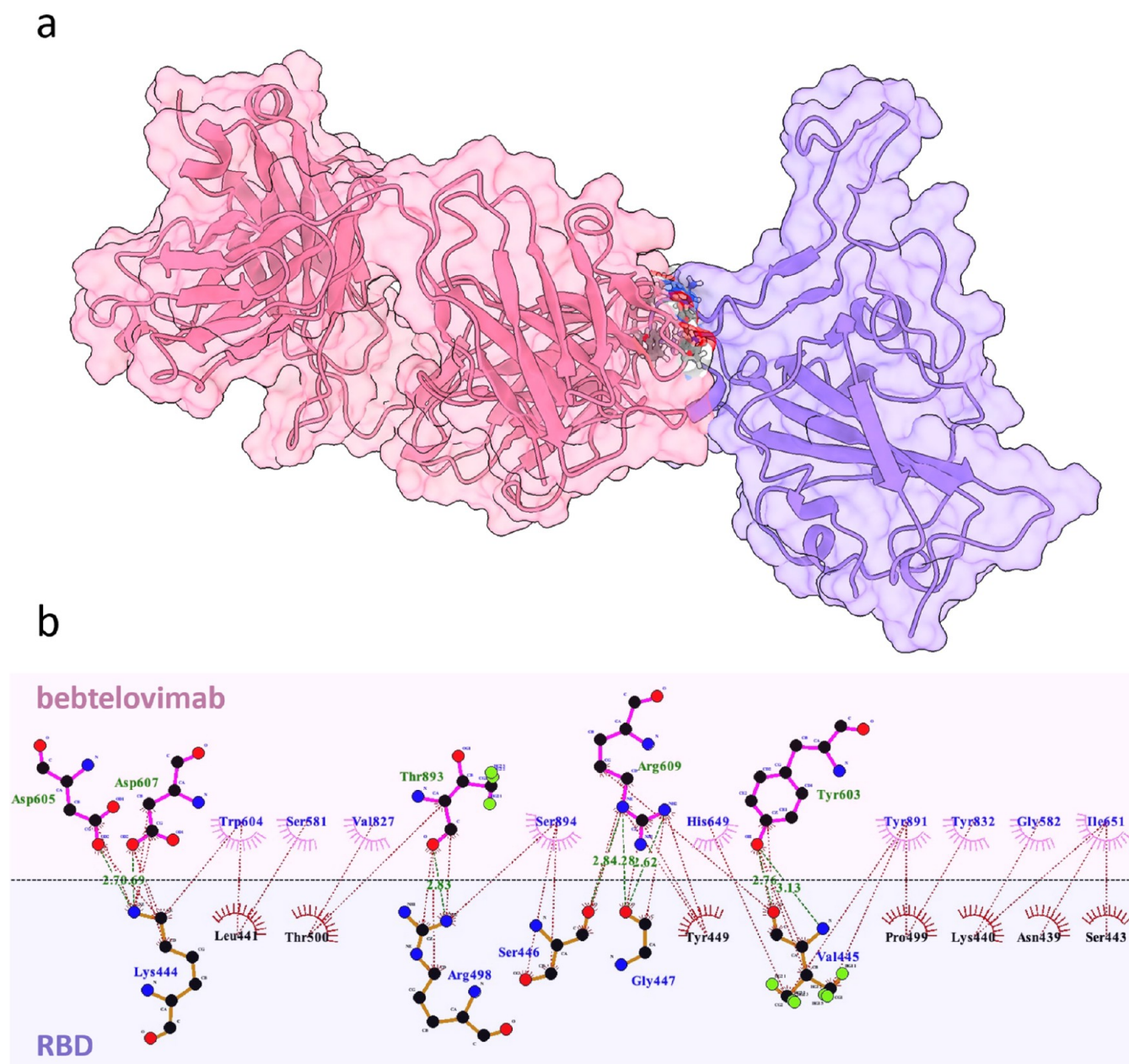


Figure 2. (a) Representative conformation of an RBD (purple)/begtelovimab (pink) complex obtained from three 100 ns explicitly solvated atomistic molecular dynamics (MD) simulations and (b) interaction network between bebtelovimab and an RBD at the binding interface.

From both the simulated MD trajectories of RBD with and without bebtelovimab binding, coordinates of all C- α atoms were extracted from every 0.1 ns of the last 30 ns of all three replicas. Time averages $A \equiv \langle A(t) \rangle$ and $G \equiv \langle G(t) \rangle$ of adjacency and communicability matrices, respectively, were then calculated from all of the timesteps. The average of the values within any submatrix elements also represented the communicability between any pairs of interested regions. In this study, a new communicability matrix containing elements G_{ij} represented the averaged communicability between pairs of α helices or β strands within the left-flank, right-flank, chest, neck, left-shoulder, and right-shoulder regions (Figure 1a) as a more simplified visualization of an allosteric signal between different protein regions through off-diagonal elements. Moreover, the difference ΔG_{ij} between each element of the communicability matrices calculated from the simulation of

RBD with and without bebtelovimab binding was defined as the “communicability gain/loss” introduced by the antibody binding, which was another mean for quantifying the allosteric signal between pairs of interested secondary structures or protein regions. The concept of communicability gain/loss was used for interpreting the effects of mutations from a protein engineering process and an evolution event at the molecular level in our previous studies.^{34,36}

3. RESULTS AND DISCUSSION

3.1. MD Simulation of RBD/Begtelovimab Interaction. Figure 2a displays the conformation of the representative RBD/begtelovimab complex obtained from the middle snapshot containing the conformation with the lowest RMSD relative to the average structure. The heavy chain region of bebtelovimab resided within the right shoulder and

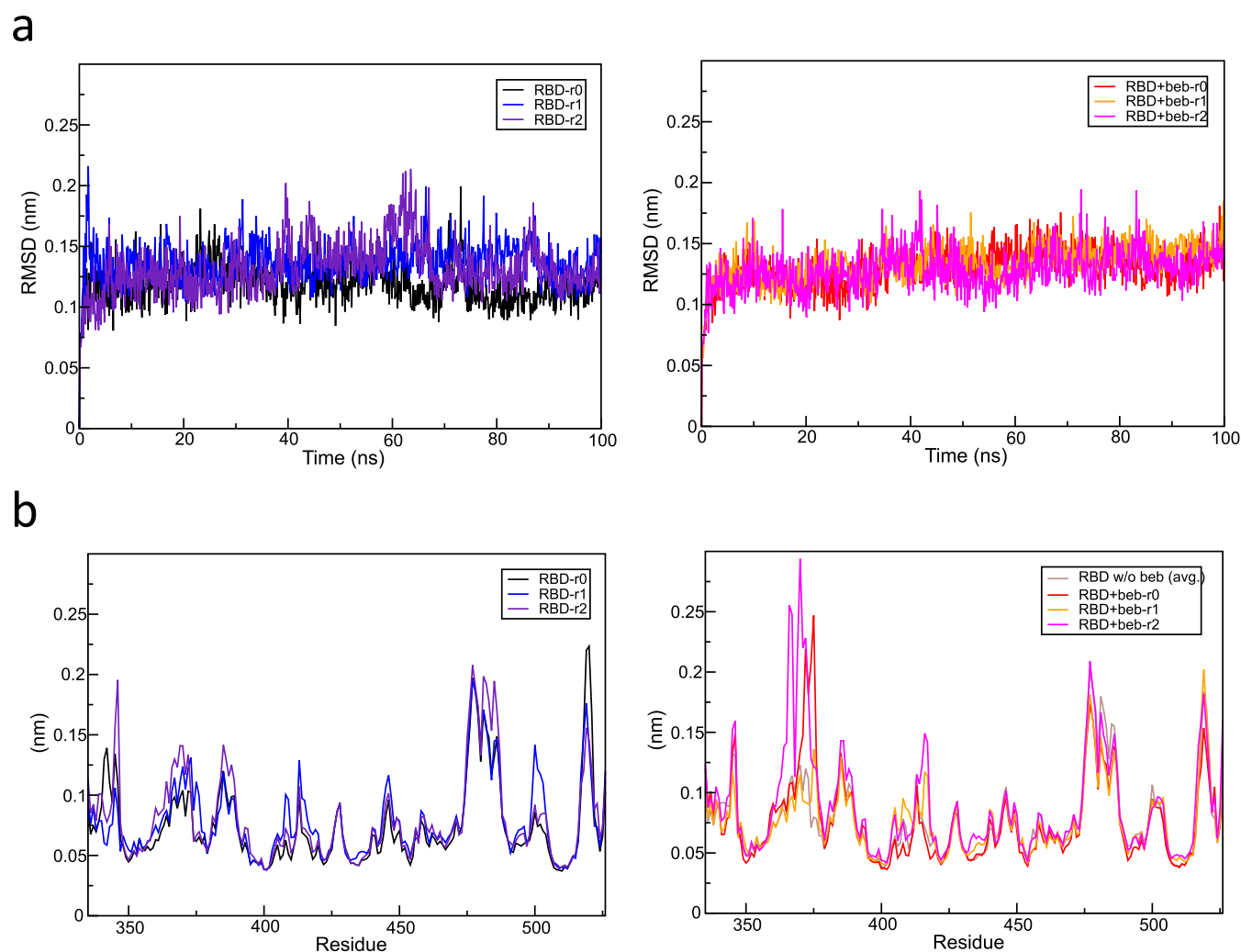


Figure 3. (a) Root-mean-square deviation (RMSD) relative to starting structures along all 100 ns MD trajectory replicas of the RBD in the absence (left) and in the presence (right) of bebtelovimab binding and (b) per-residue root-mean-square fluctuation (RMSF) of three RBD replicas in the absence (left) and in the presence (right) of bebtelovimab binding compared with the average RMSF of all replicas without bebtelovimab.

right flank regions of RBD. The interaction network between amino acids at the binding interface in Figure 2b displays five hydrogen bonds and seven residues involved in the network of hydrophobic contacts. The interaction network featured the residues 439–441 and 443 from the H7 helix, residues 498–500 from the B9/H8 loop, and the highly conserved residues 444–447 from the H7/B6 loop. The H7 helix was connected to the “chest”, while both B9/H8 loops and H7/B6 loops were connected to short β strands within the “neck” region. As the native binding interface of RBD/ACE2 during the process of viral infection mainly consisted of the left shoulder region, the neck region, and only the upper part of the right shoulder region, binding of bebtelovimab onto different RBD regions should provide an indirect inhibition mechanism that involved protein dynamics. Therefore, further analysis of the MD trajectories of an RBD both with and without bebtelovimab binding was carried out to monitor global and local conformational dynamics of RBD affected by bebtelovimab binding.

The stability of the RBD in a solvated environment was reinforced by bebtelovimab binding. The convergence of root-mean-square deviation (RMSD) calculated from all of the MD trajectories of RBD with and without bebtelovimab binding

was after 70 ns (Figure 3a). The equilibrated RMSD values were also found to be similar for RBD in the absence (0.129 ± 0.019 nm) and in the presence (0.131 ± 0.016 nm) of bebtelovimab binding. Figure 3b displays the per-residue root-mean-square fluctuation (RMSF) calculated from the last 30 ns of simulations of RBD with and without bebtelovimab binding. Peaks found in the RMSF profiles represented the regions of flexible loops, while the minima represented well-defined secondary structures, e.g., α helices and β sheets. The RBD trajectory with bebtelovimab possessed significantly higher RMSF at the H3/B3 loop of the right flank regions, which were far from the antibody binding residues identified from the interaction networks. However, bebtelovimab binding was in concurrence with lower RMSF at the B7/B8 loop of the left shoulder region opposite to the right-shoulder antibody binding site. Therefore, allosteric signals from the antibody binding sites could affect the motion of flexible loops within the receptor-binding motif (RBM) region and could, in turn, affect the RBD functions.

3.2. Generation of a Communicability Matrix from the Adjacency Matrix. To elucidate the mechanisms of RBD inhibition through the allosteric signal between the bebtelovimab binding site and a flexible loop within the ACE2

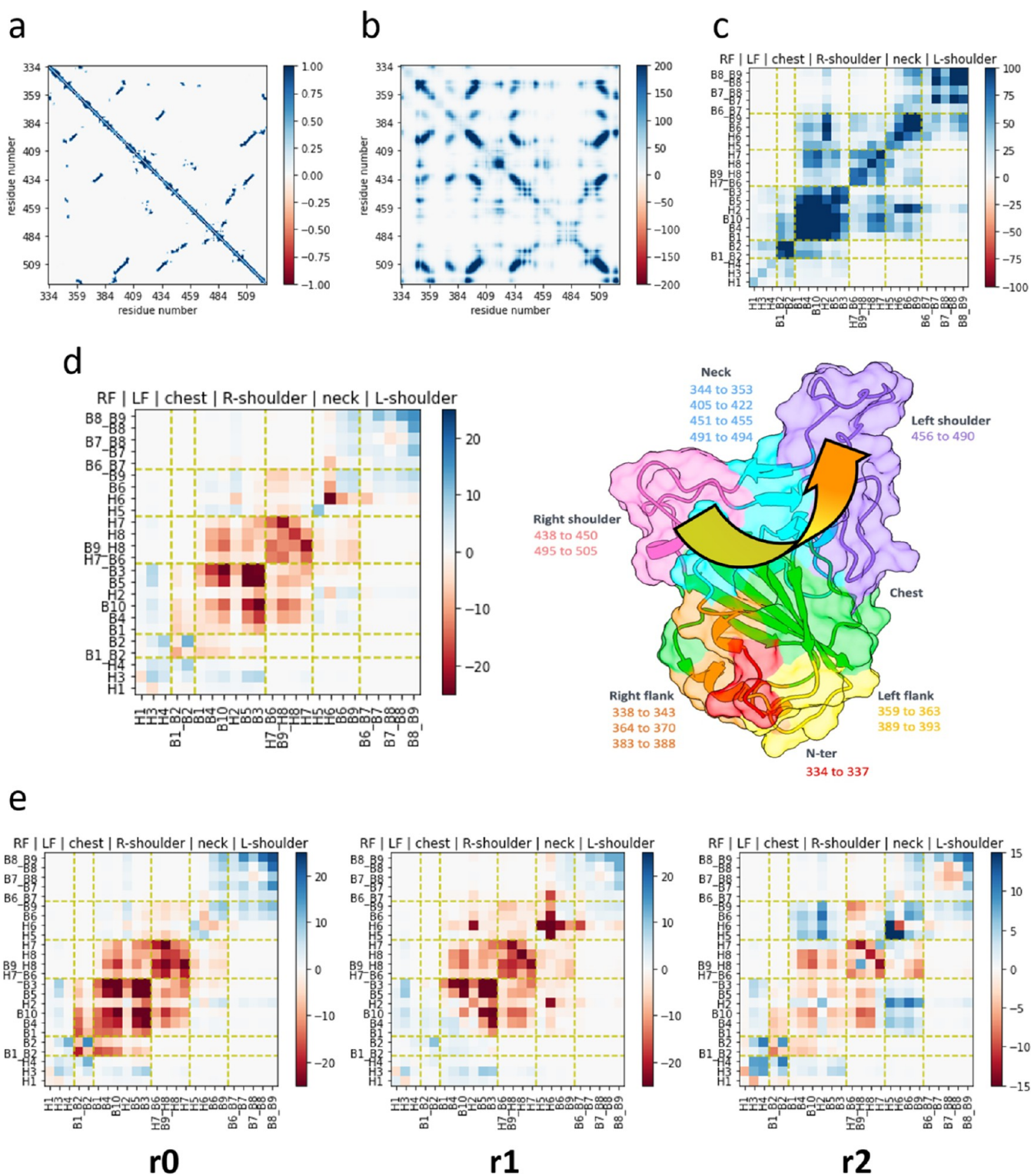


Figure 4. (a) Time-averaged adjacency matrix of an RBD domain without bebtelovimab over the last 30 ns of all three MD replicas; (b) time-averaged communicability matrix of an RBD domain without bebtelovimab; (c) communicability matrix of an RBD domain averaged over the last 30 ns of all three MD replicas and over the residues within secondary structures; (d) matrix of communicability gain/loss defined by the difference in communicability within the RBD structure without bebtelovimab binding and the RBD structure with bebtelovimab binding, averaged over three replicas; and (e) communicability gain/loss defined by the difference in communicability within the RBD structure without bebtelovimab binding and the RBD structure with bebtelovimab binding for each replica. The yellow arrow illustrates the direction of allosteric signal transfer.

receptor-binding motif (RBM) of RBD, a simple protein residue network (PRN) was defined for each snapshot of RBD trajectories through the adjacency (A) matrix described earlier in the Section 2. The existence of an “edge” between each

“node” pair of amino acid residues depended on whether the distance between the pair of representative C- α backbone atoms was smaller than the 7.4 Å cutoff. Therefore, a nonzero element within the A matrix or an edge of a PRN could both

represent a contact or a hopping of allosteric signal between a pair of nearest neighbor amino acids. As the protein conformations simulated by atomistic MD simulations were dynamic, the PRNs created for MD trajectories of proteins were also dynamic, and only the time-averaged data of A matrix element was presented.

Figure 4a displays a time-averaged adjacency matrix calculated from the last 30 ns of all three 100 ns MD trajectories of RBD without bebtelovimab binding. The nonzero $A_{i,i\pm 1}$ elements closest to the diagonal elements represented the pairs of neighboring amino acids connected through peptide bonds, while the $A_{i,i\pm 3}$ and $A_{i,i\pm 4}$ near the diagonal elements represented α helices. Considering the off-diagonal elements of the A matrix, the regions including nonzero $A_{i-n,j+n}$ were recognized as the contacts between a pair of antiparallel β -strands directly forming hydrogen bonds. Thus, nonzero elements of the A matrix signified the possibility of an allosteric signal to transfer along the axis of an α helix and between a pair of interacting β strands. Then, the communicability matrix G defined in the Section 2 as the exponential of the A matrix contained a power series of A as $G = \exp A = \hat{I} + A + A^2/2! + A^3/3! + \dots$. A nonzero element of the A^n matrix represented the number of possible hopping paths between a pair of amino acid residues, given n hopping steps. Dividing the number of paths by $n!$ represented the possible signal loss or weakening during the n -step hopping. Therefore, the time-averaged communication matrix of the simulated RBD in Figure 4b displays some additional nonzero regions that represent possible paths for the allosteric signal between nonadjacent amino acids.

3.3. Network Topology of RBD without Bebtelovimab Binding. To simplify the interpretation of matrix G , a submatrix was defined for each pair of the defined secondary structures, e.g., α helices and β strands of an RBD protein. Some important peptide loops linking pairs of secondary structures were also considered. Then, all elements in each submatrix defined between a pair of secondary structures or loops were averaged to provide the communicability score for each pair.

Figure 4c displays the matrix of the communicability score between each pair of secondary structures within the right flank (RF), left flank (LF), chest, right shoulder, neck, and left shoulder regions. Some characteristics of the RBD protein became visible, e.g., the highest communicability between all β strands within the “chest” β sheet region and relatively high communicability between secondary structures within the right shoulder, neck, and left shoulder regions. Communicability within the right flank regions was found to be relatively low as the region mainly contained flexible loops. Communicability between pairs of different regions could be observed through the off-diagonal elements, e.g., pairs between the H2 helix of the chest region and most parts of the neck region with relatively high communicability scores as they were at the interface between the two regions. A remarkable characteristic of the RBD protein was an asymmetry between the right shoulder and the left shoulder regions of RBD. The right shoulder containing the class 3 antibody epitope had a relatively high communicability with the chest and the neck regions, while the left shoulder containing three flexible loops only contained a small communicability with the neck region.

3.4. Communicability Gain/Loss of RBD Regions through Bebtelovimab Binding. After a virtual measurement and characterization of the communicability between

amino acids and secondary structures for allosteric signaling within similar and different regions of an RBD protein, the effects of bebtelovimab binding were then considered. Figure 4d,e displays a matrix of communicability gain/loss between each pair of secondary structures or loops of RBD regions upon bebtelovimab binding, which was defined through the matrix of communicability scores between the secondary structure pairs of RBD with bebtelovimab binding subtracted by that of RBD without bebtelovimab binding. While Figure 4d displays the time-averaged communicability gain/loss over all MD replicas of the RBD/bebtelovimab complex, Figure 4e displays the time averages over each replica. For all replicas of the RBD/bebtelovimab complex, a significant loss of communicability (shaded in red) was observed at the bebtelovimab binding site within the right shoulder region, which was in concurrence with the communicability loss observed between the right shoulder and the chest regions, as well as a communicability loss within the chest region. The level of communicability loss within the chest region was found to be the highest for the RBD + beb-r0 replica and was found to be the lowest for the RBD + beb-r2 replica, in which the communicability loss between the right shoulder and the neck regions became more prominent. However, the left shoulder of all RBD + beb replicas experienced a gain of communicability within the region (shaded in blue), as well as a communicability gain between the left shoulder and the neck region, especially the B6 and B9 strands at the upper part.

Considering the common characteristics of the communicability gain/loss from all MD replicas of RBD/bebtelovimab complexes, a schematic illustration of a possible path for allosteric perturbation is given by the yellow arrows in Figure 4d,e. The analysis of the RBD/bebtelovimab interaction network showed that the interactions involving H7/B6 (residue 444–450) and B9/H8 (residue 495–505) with both light and heavy chains of bebtelovimab separate both loops from each other and result in a significant loss of communicability. Interactions between H7/B6 and bebtelovimab also involved the highly conserved residues 444–447. The H7 and H8 helices were located near the B3 and B5 strands, for which a significant communicability loss was observed for the RBD + beb-r0 and RBD + beb-r1 simulations, while a slight communicability loss was observed for the same regions of RBD + beb-r2. As the B3 and B5 strands were parts of the chest region, communicability loss was also observed for the whole region, which was in concurrence with the increased RMSF or local flexibility of the H3/B3 loop observed for the RBD + beb-r0 and RBD + beb-r2 simulations. On the other hand, communicability loss within and between the H7/B6 and B9/H8 loops at the bebtelovimab binding epitope was in concurrence with the slight communicability loss between the left shoulder and the neck regions. However, the communicability between the neck and the right shoulder region increased, along with the communicability gain within the left shoulder region itself, which was reflected by the decrease of RMSF for the large flexible loop B7/B8 of the left shoulder region. This allosteric perturbation on the shoulder and neck regions of the receptor-binding motif (RBM) captured by the matrices of communicability gain/loss could affect the RBD function, as would be discussed through essential dynamics of RBD with and without bebtelovimab binding in the next section.

3.5. Consequence of the Allosteric Perturbation to the Essential Dynamics of RBD and RBM Closure.

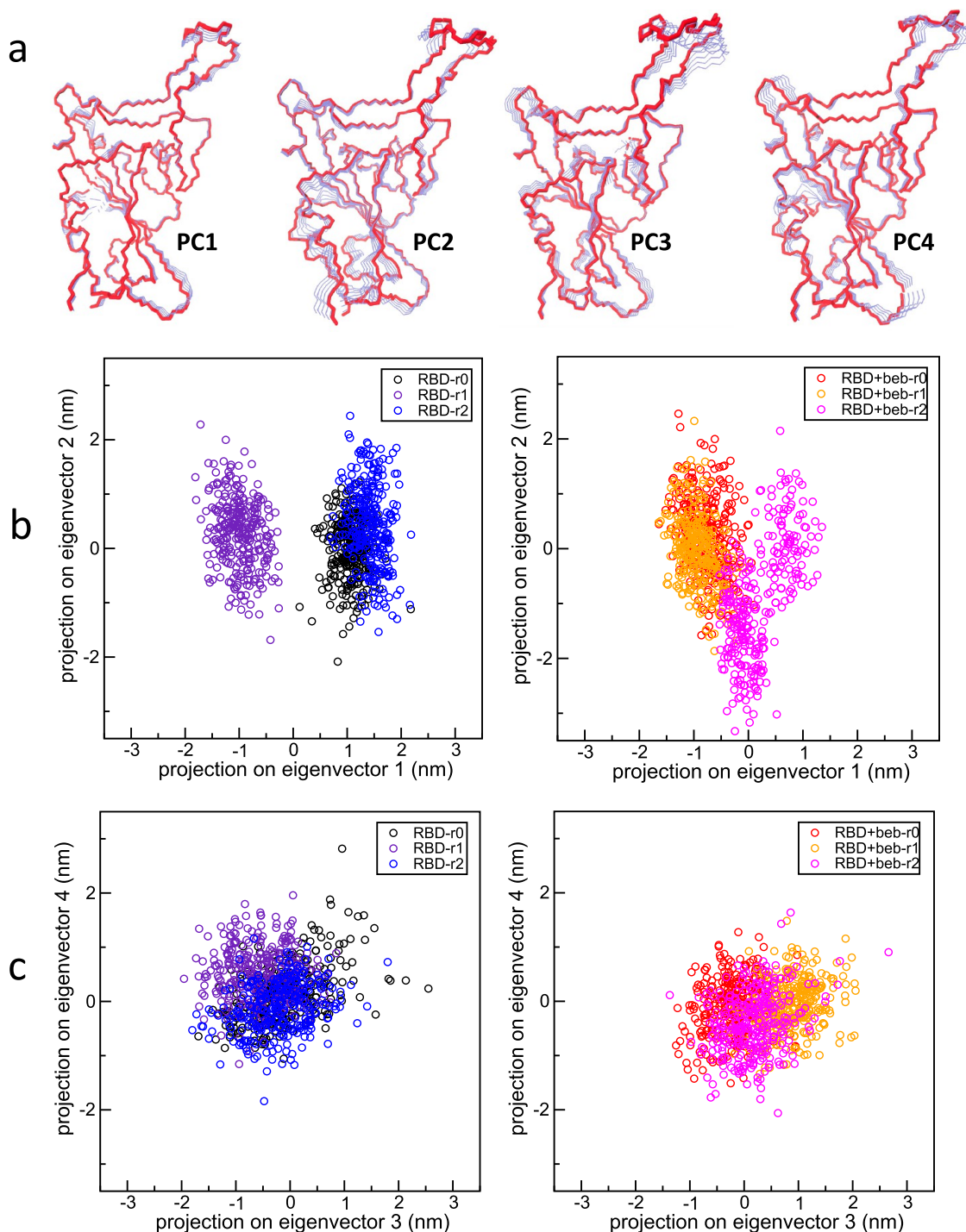


Figure 5. (a) First four essential (PCA) modes extracted from the combined RBD trajectory (the positive extremum is presented in red color), (b) projection of RBD trajectories in the absence (left) and in the presence (right) of bebtelovimab onto the first and second PCA modes, and (c) projection of RBD trajectories in the absence (left) and in the presence (right) of bebtelovimab onto the third and fourth PCA modes.

Essential dynamics of the RBD motion both with and without bebtelovimab binding was considered through principal component analysis (PCA). The equilibrated trajectories of all MD replicas of both naked RBD and the RBD/bebtelovimab complex were combined before creating a covariance matrix of all degrees of freedom for backbone atoms. The first four essential modes were extracted from the eigenvectors of the covariance matrix along with the projection of all MD trajectories on each essential mode. Figure 5a visualizes the first four principal components (PC) of RBD

motion from the combined trajectory, which highlight some important motions: PC1—flapping motion of the H3/B3 loop connected to the chest region; PC2—twisting motion of the shoulder and flank regions; PC3—closing/opening motion of the left and the right shoulders; and PC4—twisting motion of the upper part of B7/B8 loop of the left shoulder region.

Figure 5b displays the projection of all MD trajectories onto the first two essential modes (PCA1 and PCA2), in which a bimodality was observed for the flapping motion of the H3/B3 loop. RBD-r0 and RBD-r1 simulations of naked RBD were

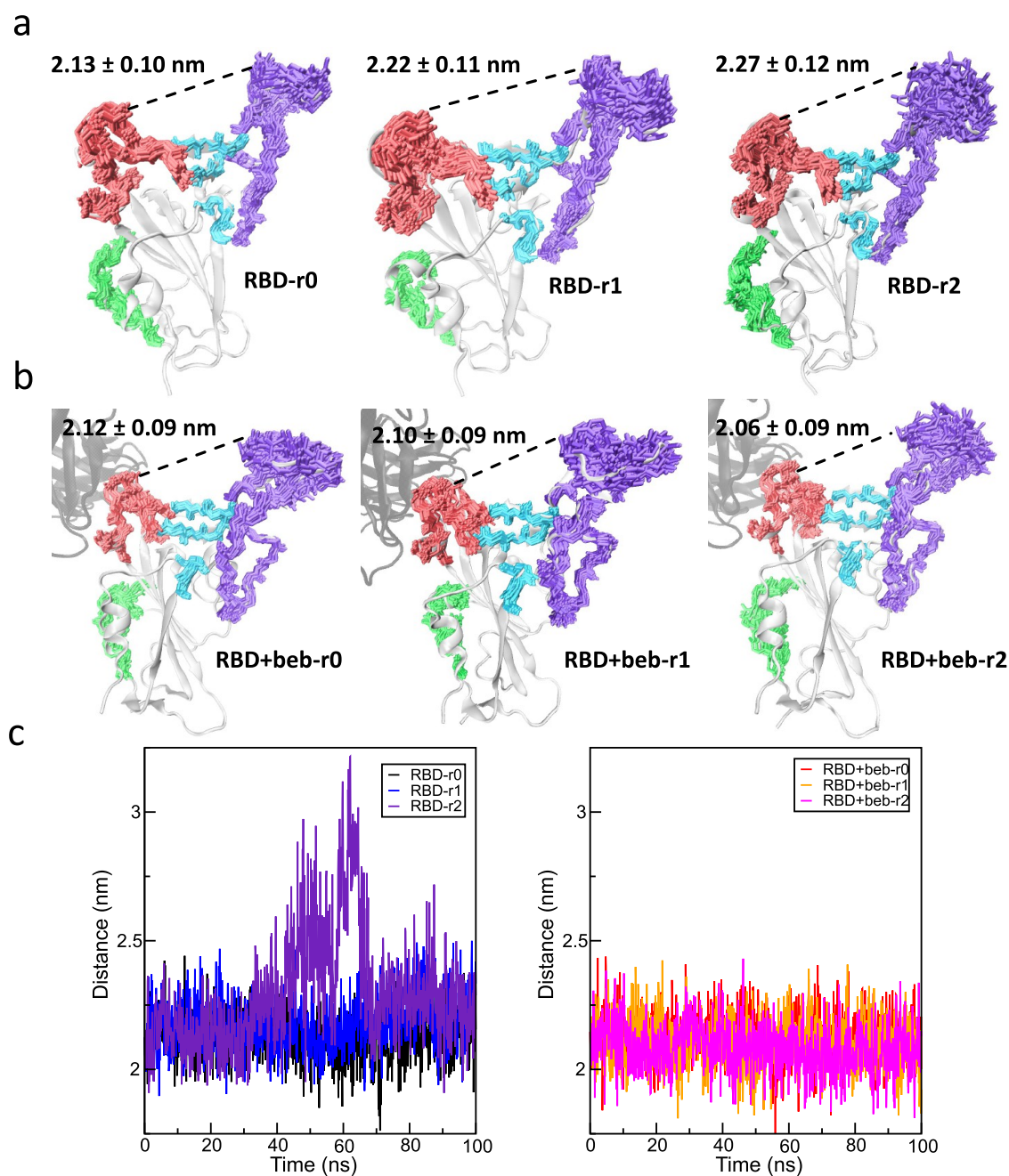


Figure 6. (a, b) Superimposed conformational snapshots of the right shoulder (pink), neck (light blue), and left shoulder (purple) regions captured every 3 ns between 70 and 100 ns for all MD replicas of RBD (a) without bebtelovimab binding and (b) with bebtelovimab binding. The yellow arrow illustrates the direction of allosteric signal transfer due to bebtelovimab binding. Solid lines were drawn between residues 446 and 484. (c) Minimum distance between residues 446 and 484 (left) without bebtelovimab binding and (right) with bebtelovimab binding.

within a positive projection of PCA1, in which the H3/B3 loop was attached to the β sheet of the chest region. For RBD-r2 and all of the RBD + beb simulations, the H3/B3 loop tended to be located away from the chest region, corresponding with the observed high RMSF and the communicability loss. The twisting motion of PCA2 was common for all simulations with and without bebtelovimab binding except for a bimodality observed for the RBD + beb-r2 simulation, where the H3/B3 helix became unfolded and fluctuated and the B7/B8 loop of the right shoulder region became twisted toward the two α helices of the left shoulder region.

Closure of the receptor-binding motif (RBM) gate or space between the left and the right shoulders of RBD became more

prominent for the PC3 and PC4 modes (Figure 5c), where the RBM gates from all RBD simulations with bebtelovimab binding displayed a higher tendency to close than those from RBD simulations without bebtelovimab binding. The RBM gate motion was further visualized through the superimposed snapshots in Figure 6a,b and the measurement of the minimum distance between residue 446 of the right shoulder region and residue 484 of the left shoulder region. The communicability gain between the β strands of the neck region and the left shoulder region was in concurrence with their improved stability and lower RMSF, causing the tip of the B7/B8 loop to remain intact with the B7 and B8 strands. Therefore, a slightly shorter distance between the residues 446 and 484 was

observed for all MD replicas of RBD with bebtelovimab binding.

Bebtelovimab stabilized the right shoulder region of the RBD but disrupted the amino acid interaction network, causing a communicability loss at the chest region but a communicability gain between the neck and left shoulder regions. A similar phenomenon was interpreted as the entropy transfer via allosteric communication in a previous study.³⁷ As the system was equilibrated, the entropy should be conserved through the transfer of conformational fluctuation and communicability loss/gain. Therefore, as the communicability loss was observed for some RBD regions, the communicability gain was also observed in the other regions. The resulting “closed” conformation of the RMB “gate” could prevent the ACE2 receptor binding at the early viral infection stage upon the allosteric signal provided by a class 3 antibody binding.

4. CONCLUSIONS

This study investigates the inhibitory mechanism of a class 3 monoclonal antibody (mAb) on the ACE2 receptor-binding domain (RBD) of SARS-CoV-2 by using atomistic molecular dynamics (MD) simulations. The simulations, conducted with and without a specific bebtelovimab mAb, revealed that bebtelovimab stabilizes flexible loops in the RBD’s epitope region, disrupting the nearby interaction network and resulting in a conformation that prevents ACE2 binding. Understanding this allosteric action holds promise for developing alternative mAbs against emerging variants of concern. The communicability matrix and the communicability gain/loss matrix are highlighted as valuable computational tools to visualize and comprehend the effects of allostery, aiding in pinpointing potential allosteric signal transfer sites. These insights may advance allostery research and its applications along with other allostery quantification techniques.³⁸

AUTHOR INFORMATION

Corresponding Author

Thana Sutthibutpong – *Theoretical and Computational Physics Group, Department of Physics, Faculty of Science and Center of Excellence in Theoretical and Computational Science (TACS-CoE), Faculty of Science, King Mongkut’s University of Technology Thonburi, Bangkok 10140, Thailand*; orcid.org/0000-0002-4468-8885; Email: thana.sut@kmutt.ac.th

Authors

Patamalai Boonserm – *Department of Microbiology, Faculty of Science, King Mongkut’s University of Technology Thonburi, Bangkok 10140, Thailand*

Wasusit Somsoros – *Department of Microbiology, Faculty of Science, King Mongkut’s University of Technology Thonburi, Bangkok 10140, Thailand*

Pongsak Khunrae – *Department of Microbiology, Faculty of Science, King Mongkut’s University of Technology Thonburi, Bangkok 10140, Thailand*

Krit Charupanit – *Department of Biomedical Sciences and Biomedical Engineering, Faculty of Medicine, Prince of Songkla University, Songkhla 90110, Thailand*

Praopim Limsakul – *Division of Physical Science, Faculty of Science and Center of Excellence for Trace Analysis and Biosensor (TAB-CoE), Faculty of Science, Prince of Songkla University, Songkhla 90110, Thailand*

Complete contact information is available at:

<https://pubs.acs.org/10.1021/acsomega.3c07947>

Notes

The authors declare no competing financial interest.

ACKNOWLEDGMENTS

This research was supported by the National Science, Research, and Innovation Fund (NSRF) and the Prince of Songkla University (Grant No. SCI6505060S). Patamalai Boonserm was supported by the Petchra Pra Jom Klao Ph.D. Research Scholarship from King Mongkut’s University of Technology Thonburi, under grant agreement number 72/2563.

REFERENCES

- (1) Kim, S.-M.; Kim, E. H.; Casel, M. A. B.; et al. SARS-CoV-2 variants with NSP12 P323L/G671S mutations display enhanced virus replication in ferret upper airways and higher transmissibility. *Cell Rep.* **2023**, *42* (9), No. 113077.
- (2) Zhou, H.; Møhlenberg, M.; Thakor, J. C.; et al. Sensitivity to Vaccines, Therapeutic Antibodies, and Viral Entry Inhibitors and Advances To Counter the SARS-CoV-2 Omicron Variant. *Clin. Microbiol. Rev.* **2022**, *35* (3), No. e00014-22.
- (3) Jackson, C. B.; Farzan, M.; Chen, B.; et al. Mechanisms of SARS-CoV-2 entry into cells. *Nat. Rev. Mol. Cell Biol.* **2022**, *23* (1), 3–20.
- (4) Fehr, A. R.; Perlman, S. Coronaviruses: an overview of their replication and pathogenesis. *Methods Mol. Biol.* **2015**, *1282*, 1–23.
- (5) Basavarajappa, S. C.; Liu, A. R.; Bruchez, A.; et al. Trimeric receptor-binding domain of SARS-CoV-2 acts as a potent inhibitor of ACE2 receptor-mediated viral entry. *iScience* **2022**, *25* (8), No. 104716.
- (6) Kakavandi, S.; Zare, I.; Vaezjalali, M.; et al. Structural and non-structural proteins in SARS-CoV-2: potential aspects to COVID-19 treatment or prevention of progression of related diseases. *Cell Commun. Signaling* **2023**, *21* (1), 110.
- (7) Banerjee, S.; Wang, X.; Du, S.; et al. Comprehensive role of SARS-CoV-2 spike glycoprotein in regulating host signaling pathway. *J. Med. Virol.* **2022**, *94* (9), 4071–4087.
- (8) Pogue, J. M.; Lauring, A. S.; Gandhi, T. N. et al. Monoclonal Antibodies for Early Treatment of COVID-19 in a World of Evolving SARS-CoV-2 Mutations and Variants. In *Open Forum Infectious Diseases*; Oxford University Press: US, 2021; Vol. 8ofab268 DOI: [10.1093/ofid/ofab268](https://doi.org/10.1093/ofid/ofab268).
- (9) Focosi, D.; McConnell, S.; Casadevall, A.; et al. Monoclonal antibody therapies against SARS-CoV-2. *Lancet Infect. Dis.* **2022**, *22* (11), e311–e326.
- (10) Gruell, H.; Vanshylla, K.; Weber, T.; et al. Antibody-mediated neutralization of SARS-CoV-2. *Immunity* **2022**, *55* (6), 925–944.
- (11) Yi, C.; Sun, X.; Ling, Z.; et al. Jigsaw puzzle of SARS-CoV-2 RBD evolution and immune escape. *Cell. Mol. Immunol.* **2022**, *19* (7), 848–851.
- (12) Laiton-Donato, K.; Franco-Muñoz, C.; Álvarez-Díaz, D. A.; et al. Characterization of the emerging B.1.621 variant of interest of SARS-CoV-2. *Infect., Genet. Evol.* **2021**, *95*, No. 105038, DOI: [10.1016/j.meegid.2021.105038](https://doi.org/10.1016/j.meegid.2021.105038).
- (13) Chen, K. W.; Huang, D. T.; Huang, L.-M. SARS-CoV-2 variants – Evolution, spike protein, and vaccines. *Biomed. J.* **2022**, *45* (4), 573–579.
- (14) Zhou, D.; Ren, J.; Fry, E. E.; et al. Broadly neutralizing antibodies against COVID-19. *Curr. Opin. Virol.* **2023**, *61*, No. 101332.
- (15) Chen, Y.; Zhao, X.; Zhou, H.; et al. Broadly neutralizing antibodies to SARS-CoV-2 and other human coronaviruses. *Nat. Rev. Immunol.* **2023**, *23* (3), 189–199.
- (16) Deshpande, A.; Harris, B. D.; Martinez-Sobrido, L.; et al. Epitope Classification and RBD Binding Properties of Neutralizing

Antibodies Against SARS-CoV-2 Variants of Concern. *Front. Immunol.* **2021**, *12*, 691715 DOI: 10.3389/fimmu.2021.691715.

(17) Jensen, J. L.; Sankhala, R. S.; Dussupt, V.; et al. Targeting the Spike Receptor Binding Domain Class V Cryptic Epitope by an Antibody with Pan-Sarbecovirus Activity. *J. Virol.* **2023**, *97* (7), No. e01596-22.

(18) Alcantara, M. C.; Higuchi, Y.; Kirita, Y.; et al. Deep Mutational Scanning to Predict Escape from Bebtelovimab in SARS-CoV-2 Omicron Subvariants. *Vaccines* **2023**, *11* (3), 711.

(19) Sridhara, S.; Gungor, A. B.; Erol, H. K.; et al. Lack of effectiveness of Bebtelovimab monoclonal antibody among high-risk patients with SARS-Cov-2 Omicron during BA.2, BA.2.12.1 and BA.5 subvariants dominated era. *PLoS One* **2023**, *18* (4), No. e0279326.

(20) Cao, Y.; Yisimayi, A.; Jian, F.; et al. BA.2.12.1, BA.4 and BA.5 escape antibodies elicited by Omicron infection. *Nature* **2022**, *608* (7923), 593–602.

(21) Cele, S.; Jackson, L.; Khoury, D. S.; et al. Omicron extensively but incompletely escapes Pfizer BNT162b2 neutralization. *Nature* **2022**, *602* (7898), 654–656.

(22) Bruel, T.; Hadjadj, J.; Maes, P.; et al. Serum neutralization of SARS-CoV-2 Omicron sublineages BA.1 and BA.2 in patients receiving monoclonal antibodies. *Nat. Med.* **2022**, *28* (6), 1297–1302.

(23) Harvey, W. T.; Carabelli, A. M.; Jackson, B.; et al. SARS-CoV-2 variants, spike mutations and immune escape. *Nat. Rev. Microbiol.* **2021**, *19* (7), 409–424.

(24) Westendorf, K.; Žentelis, S.; Wang, L.; et al. LY-CoV1404 (bebtelovimab) potently neutralizes SARS-CoV-2 variants. *Cell Rep.* **2022**, *39* (7), No. 110812.

(25) Tan, Z. W.; Tee, W. V.; Samsudin, F.; et al. Allosteric perspective on the mutability and druggability of the SARS-CoV-2 Spike protein. *Structure* **2022**, *30* (4), 590–607.e4.

(26) Lan, J.; Ge, J.; Yu, J.; et al. Structure of the SARS-CoV-2 spike receptor-binding domain bound to the ACE2 receptor. *Nature* **2020**, *581* (7807), 215–220.

(27) Westendorf, K.; et al. LY-CoV1404 (bebtelovimab) potently neutralizes SARS-CoV-2 variants. *Cell Rep.* **2022**, *39* (7), No. 110812, DOI: 10.1016/j.celrep.2022.110812.

(28) Berman, H. M.; et al. The Protein Data Bank. *Nucleic Acids Res.* **2000**, *28*, 235–242, DOI: 10.1093/nar/28.1.235.

(29) Van Der Spoel, D.; Lindahl, E.; Hess, B.; et al. GROMACS: fast, flexible, and free. *J. Comput. Chem.* **2005**, *26* (16), 1701–1718.

(30) Oostenbrink, C.; Villa, A.; Mark, A. E.; et al. A biomolecular force field based on the free enthalpy of hydration and solvation: The GROMOS force-field parameter sets 53A5 and 53A6. *J. Comput. Chem.* **2004**, *25* (13), 1656–1676.

(31) Bussi, G.; Donadio, D.; Parrinello, M. Canonical sampling through velocity rescaling. *J. Chem. Phys.* **2007**, *126* (1), No. 014101, DOI: 10.1063/1.2408420.

(32) Lin, Y.; Pan, D.; Li, J.; et al. Application of Berendsen barostat in dissipative particle dynamics for nonequilibrium dynamic simulation. *J. Chem. Phys.* **2017**, *146* (12), No. 124108, DOI: 10.1063/1.4978807.

(33) Wallace, A. C.; Laskowski, R. A.; Thornton, J. M. LIGPLOT: a program to generate schematic diagrams of protein-ligand interactions. *Protein Eng., Des. Sel.* **1995**, *8* (2), 127–134, DOI: 10.1093/protein/8.2.127.

(34) Sawang, N.; Phongphanphanee, S.; Wong-ekkabut, J.; et al. Biophysical Interpretation of Evolutionary Consequences on the SARS-CoV2Main Protease through Molecular Dynamics Simulations and Network Topology Analysis. *J. Phys. Chem. B* **2023**, *127* (11), 2331–2343.

(35) Arrigo, F.; Durastante, F. Mittag-Leffler Functions and their Applications in Network Science. *SIAM J. Matrix Anal. Appl.* **2021**, *42* (4), 1581–1601, DOI: 10.1137/21M1407276.

(36) Sutthibutpong, T.; Muhammad, A.; Sawang, N.; et al. Effects of Site-Directed Mutations on the Communicability between Local Segments and Binding Pocket Distortion of Engineered GH11 Xylanases Visualized through Network Topology Analysis. *Catalysts* **2022**, *12* (10), 1165.

(37) Hacisuleyman, A.; Erman, B. Entropy Transfer between Residue Pairs and Allostery in Proteins: Quantifying Allosteric Communication in Ubiquitin. *PLoS Comput. Biol.* **2017**, *13* (1), No. e1005319.

(38) Singh, S.; Bowman, G. R. Quantifying Allosteric Communication via Both Concerted Structural Changes and Conformational Disorder with CARDS. *J. Chem. Theory Comput.* **2017**, *13* (4), 1509–1517.